Transverse Patterns and Dual-Frequency Lasing in a Low-Noise Nonplanar-Ring Orbital-Angular-Momentum Oscillator

Yaqin Cao,[1] Ping Liu,[1] Cuifang Hou,[1] Yanne K. Chembo⬤,[2] Zehuang Lu,[1] and Guoping Lin⬤[1,3,*]

[1] *MOE Key Laboratory of Fundamental Physical Quantities Measurement, Hubei Key Laboratory of Gravitation and Quantum Physics, PGMF and School of Physics, Huazhong University of Science and Technology, Wuhan 430074, China*

[2] *Institute for Research in Electronics and Applied Physics (IREAP), and Department of Electrical and Computer Engineering, University of Maryland, College Park, Maryland 20742, USA*

[3] *Ministry of Industry and Information Technology Key Lab of Micro-Nano Optoelectronic Information System, School of Science, Harbin Institute of Technology, Shenzhen 518055, China*

Monolithic optical cavities employing total internal reflections are appealing compact platforms for a wide range of applications from fundamental physics to industry applications. We characterize the transverse patterns of a millimeter-size monolithic nonplanar ring vortex laser pumped by a Gaussian beam. Vortex beams carrying orbital angular momentum (OAM) up to 30 together with vortex crystals and petal patterns are observed. The rigid nature of the monolithic cavity brings along its low-noise lasing performance for these beams. A frequency noise floor as low as $0.1 \ \mathrm{Hz/Hz^{1/2}}$ corresponding to sub-Hz instantaneous linewidth is measured. Furthermore, we demonstrate low-noise dual-frequency lasing with phase noise as low as $-118 \ \mathrm{dBc/Hz}$ at 10-kHz offset for the beatnote at 8.2 GHz. We expect that such versatile and compact OAM laser sources can facilitate multiple applications including optical communications, optical tweezers, and laser metrology such as dual-frequency Doppler lidar.

I. INTRODUCTION

Vortex light beams are typically referred to as beams with helical wavefronts, in which the associated singularity points lead to zero intensity or dark spots in transverse beam profiles. These beams are found to carry orbital angular momentum (OAM) of light [1], an interesting feature that has brought an additional dimension to characterize and manipulate light beams. To date, a wide range of applications have been established using this characteristic of light [2–10]. For instance, optical communication employing OAM multiplexing is demonstrated [11] and terabit-scale data transmission in both free space and fibers have been reported [12,13]. Vortex light used in a single-photon high-dimensional quantum key distribution system for intracity quantum cryptography has also been recently demonstrated [14]. OAM states for high-dimensional quantum communication using an air-cored fiber is explored [15]. Tremendous experiments using vortex light beams have been carried out in various fields such as other quantum techniques [16–19], optical manipulation [20], superresolution optical microscopy [21], laser material processing [22,23], and precision measurements such as angstrom localization of nanoantennas [24].

Generation of coherent vortex beams carrying OAM can be performed both external and internal to laser cavities [25–28]. Numerous techniques have been developed to convert a regular Gaussian laser beam into a vortex beam, which can rely on a pair of astigmatic lens [29], gradient index lens cascades [30], a spiral-phase plate [31], holographic elements [32], liquid-crystal elements [33] including Q plates [34], metasurfaces [35,36], and other nanophotonic elements [37–39], to mention a few. Active devices for the creation of desired vortex beams using liquid-crystal spatial-light modulators (SLM) [40], and digital micromirror devices (DMD) [41] are reported. On the other hand, vortex beams can also be directly generated inside a laser cavity. The aforementioned elements can be used to form a vortex laser mode. For instance, an intracavity SLM as a digital mirror can output on-demand vortex laser beams [42]. On-chip microring OAM lasers with complex refractive-index modulation patterns have been reported [43]. Recently, it is also found that intracavity microspheres in a Fabry-Perot (FP) laser can emit vortex beams [44]. Regarding laser cavities that naturally host Laguerre-Gaussian (LG) modes, one can selectively excite them by either manually adding losses to the unwanted modes or by tilting or shaping the pump beam to create preferred gain profiles for vortex modes [25,27]. For instance, high order LG vortex lasing up to 288th is demonstrated

---

*[*]guoping.lin@hotmail.com

with inscribed defect patterns on the surface of the output coupler [45].

Although additional intracavity optical elements can enable better control over OAM lasing, they inevitably induce losses to the cavity, which could be an obstacle for the direct generation of narrow-linewidth continuous-wave laser beams. Millimeter-size (mm-size) monolithic optical platforms based on successive total internal reflections (TIRs) [46], on the other hand, can transfer very low-noise performance to lasing beams. High-quality factor whispering-gallery mode cavity using a large amount of TIRs has been a well-known example for investigating various nonlinear frequency conversion phenomena [47–49]. Another type of mm-size monolithic cavities are the so-called nonplanar ring cavities, in which light is confined through a few TIRs within one roundtrip. A well-designed high-reflection coating at one facet of this kind of cavity is often used to facilitate free-space beam coupling [50,51]. Solid-state lasers adopting this kind of monolithic nonplanar ring configuration are known to feature narrow-linewidth and rigid performance, which have favored successful applications in precision measurements such as the ground-based Laser Interferometer Gravitational-Wave Observatory (LIGO) [52] and the gravity recovery and climate experiment space mission (GRACE Follow-On) [53].

The rotation of beam profile in the nonplanar ring-cavity configuration results in the support of high-order Laguerre-Gaussian modes including vortex beams [54]. This feature has been recently employed for studying synthetic Landau levels for photons using a four-mirror resonator [55] and investigated for potential improvement to future gravitational-wave detectors [56,57]. Here, we report the direct generation of vortex beams with topological charge up to 30 from a monolithic nonplanar ring cavity made of Nd:YAG. We investigate the transverse patterns of such an OAM oscillator through varying the relative pump-beam position on the coupling facet. Mode indices are determined using a tilted biconvex spherical lens and an imaging device. Low-noise single-frequency vortex beam lasing with the frequency noise floor as low as 0.1 Hz/Hz$^{1/2}$ is demonstrated indicating a sub-Hz level instantaneous linewidth. We also show that very low-noise dual-frequency lasing can be realized in such a compact cavity. The phase noise of a dual-frequency beat signal at 8.2 GHz reaches −118 dBc/Hz at 10-kHz offset frequency. Our findings show that vortex beams emitted from a monolithic nonplanar ring cavity feature low-noise performance and are attractive highly coherent laser sources for various precision-measurement applications.

II. EXPERIMENTAL SETUP

The schematic of the experimental setup to realize and characterize the nonplanar ring vortex laser is illustrated in
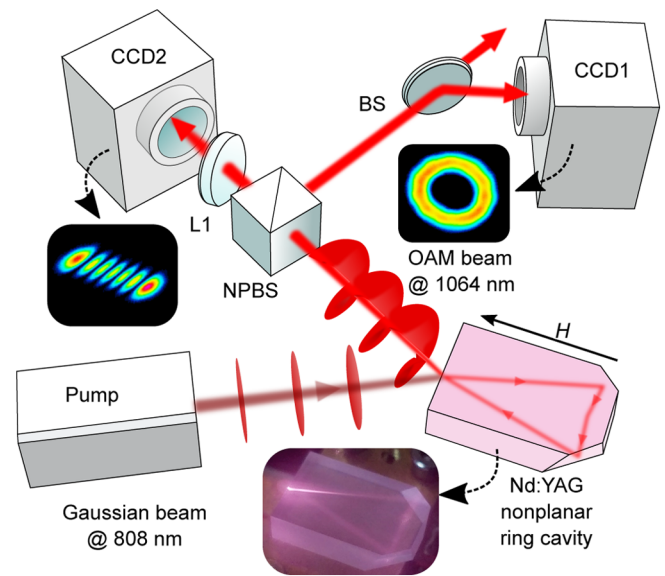

FIG. 1. Schematic of the experimental setup. NPBS, nonpolarizing beam splitter; BS, beam splitter; L1, biconvex spherical lens; CCDs, digital cameras. Insets: a picture of the laser cavity in operation and recorded beam profiles with and without passing a tilted lens L1.

Fig. 1. The cavity made of Nd:YAG crystal, as shown in the inset, has a dimension of $3 \times 8 \times 12 \, mm^3$. Its dopant concentration is about 0.8%. The ring cavity confines light beams through three total internal reflections and one reflection at a coated facet within one roundtrip. The coating is designed to feature antireflection for the pump at 808 nm and high reflection for the lasing at 1064 nm. The nonplanar roundtrip of light enables stable and single directional emission [50,58,59]. It is realized by creating loss differences between clockwise and counter-clockwise modes using Faraday effect in the presence of an external magnetic field. Here we use a pair of Nd-Fe-B permanent magnets to provide the required magnetic field.

The pump laser source is a single-mode fiber-Bragg-grating- (FBG) stabilized diode laser with continuous-wave output power typically up to 250 mW. It is focused on the input facet of the cavity at the designed incident angle of about 30°. The relative position of the pump beam is controllable by mounting the cavity on a two-dimensional translation stage. The pump beam emitted from the fiber pigtail is characterized with a Gaussian profile, illustrated by plane wavefronts in the figure. From the photograph of the crystal, one sees a decaying pump beam when it enters the crystal, which is due to the absorption from the four-level energy structure of Nd ions. The luminescence at 1064 nm is captured in this photograph, showing the traveling-wave roundtrip of lasing beams in the cavity formed by three total internal reflections and one refection at the coated facet. The vortex lasing featuring a helical

wavefront is also illustrated in the setup. The lasing wavelength is tunable through adjusting the temperature and the stress applied on the monolithic cavity.

The original beam profile of the emitted light is recorded using a CCD (CCD1). To characterize mode orders including topological charges of emitted light beams carrying OAM, we employ the simple and efficient method based on a tilted biconvex spherical lens (L1) and another camera (CCD2) [60]. The lens has a focal length of 50 mm. Examples of beam profiles for a vortex beam are provided in the insets. The lasing performance is also monitored using a scanning Fabry-Perot interferometer. We also couple the free-space beam into a single-mode fiber for further characterization including examining its single- and dual-frequency performance with an optical spectrum analyzer (Yokogawa AQ6373B). The lasing signals are down-converted to the rf domain using a fiber-pigtailed fast photodetector (ALPHALAS UPD-15-IR2-FC). Subsequently, the frequency noise spectrum is studied by analyzing rf signals using the signal spectrum and phase-noise analyzers (R&S FSW26 and R&S FSWP26).

III. TRANSVERSE PATTERNS

The nonplanar configuration of the optical cavity not only allows for single directional lasing, but also paves a possible way to compensate the astigmatism of the cavity. Its polarization rotation property in confined light beams typically leads to a nearly circularly polarized laser signal output, which is observed in our experiment using a polarization analyzer (Schäfter + Kirchhoff SK010PA). On the other hand, the image rotation in the laser roundtrip leads to Laguerre-Gaussian-like modes. The complex amplitude of LG modes can be expressed as [2]

$$
\mathrm{LG}_{p\ell}(r,z,\phi) = \sqrt{\frac{2p!}{\pi(p+|\ell|)!}} \frac{1}{w(z)} \left[\frac{r\sqrt{2}}{w(z)}\right]^{|\ell|} \mathrm{L}_p^{|\ell|}\left[\frac{2r^2}{w^2(z)}\right]
$$
$$
\times \exp\left[\frac{-r^2}{w^2(z)}\right] \exp\left[\frac{ik_0 r^2}{2R(z)}\right] \exp(i\ell\phi)
$$
$$
\times \exp\left[-i(2p+|\ell|+1)\arctan\left(\frac{z}{z_R}\right)\right],
$$
$$(1)$$

where ℓ is the topological charge defining the degree of twisting for the wavefront, p denotes the number of nodes in the radial direction of the intensity distribution, $w(z)$ is the radius of the beam at z position along the propagation direction, z_R is the Rayleigh range, $R(z)$ is the radius of curvature, w_0 is the beam waist, and $k_0 = 2\pi/\lambda$ is the wavenumber. Here, $\mathrm{L}_p^{|\ell|}$ are the generalized Laguerre polynomials.

To investigate a variety of transverse patterns of the emitted OAM light beams, relative position of the focused Gaussian pump beam on the cavity is controlled using a translation stage. Different lasing modes can be excited depending on mode overlap and mode-competition conditions. We first locate the optimal position of the pump for maximum laser-power output, where the fundamental Gaussian mode (TEM$_{00}$ or LG$_{00}$) lases. It should be noted that this position is usually at the center of the facet for a precisely machined cavity. We then map out the positions where various transverse emission patterns are observed. An example of the relative positions of the pump beam on the cavity for several lasing modes is plotted (see Appendix A).

Figure 2(a) shows the illustration of the relative positions of the pump beam on the cavity and example photographs of the cavity when lasing occurs on the fundamental mode and the high-order LG mode. One can clearly observe the expected widening of the lasing beam inside the cavity when high-order-mode lasing occurs in comparison with that of the fundamental lasing. By carefully examining the original emission patterns in CCD1, various LG lasing modes are found. Figure 2(b) provides the observed LG$_{00}$, LG$_{10}$, LG$_{20}$, LG$_{11}$, and LG$_{12}$ modes, from which one sees the mode number p presenting the nodes of the light-intensity distribution in the radial direction. Vortex beams with LG mode numbers $p = 0$ and $\ell \neq 0$ are also recorded as shown in Fig. 2(c).

To determine the topological charge ℓ, we employ the simple method based on a tilted biconvex spherical lens as the single conversion element [60]. The converted beam profiles after the lens at an optimal position slightly shifted from the focus are recorded in CCD2. As shown in Figs. 2(b) and 2(c), the converted profiles are characterized with spatially distributed intensity spots, which are related to mode indices of lasing beams. The converted profile in CCD2 can be theoretically studied using the generalized Huygens-Fresnel integral [60]. Here, the complex electric field after passing through the tilted lens can be calculated by

$$
E_2(x_2, y_2) = \frac{i/\lambda}{|B|^{1/2}} \int \int dx_1 dy_1 E_1(x_1, y_1) e^{-(i\pi/\lambda)\phi(\mathbf{r_1, r_2})},
$$
$$(2)$$

where $E_{1,2}$ represent the complex electric fields at the waist position before the lens and at a further distance z after passing the lens, respectively. The parameters B and $\phi(\mathbf{r_1, r_2})$ can be obtained from the ABCD transfer matrix of the system. When the camera is placed at the optimal position after the lens, the converted beam profiles then provide the information of mode indices.

We numerically calculate the converted images from various ideal LG modes by using Eqs. (1) and (2). The results are also presented in Figs. 2(b) and 2(c) showing a good agreement with the experimental data. One observes that the number of the intensity spot arrays gives the value
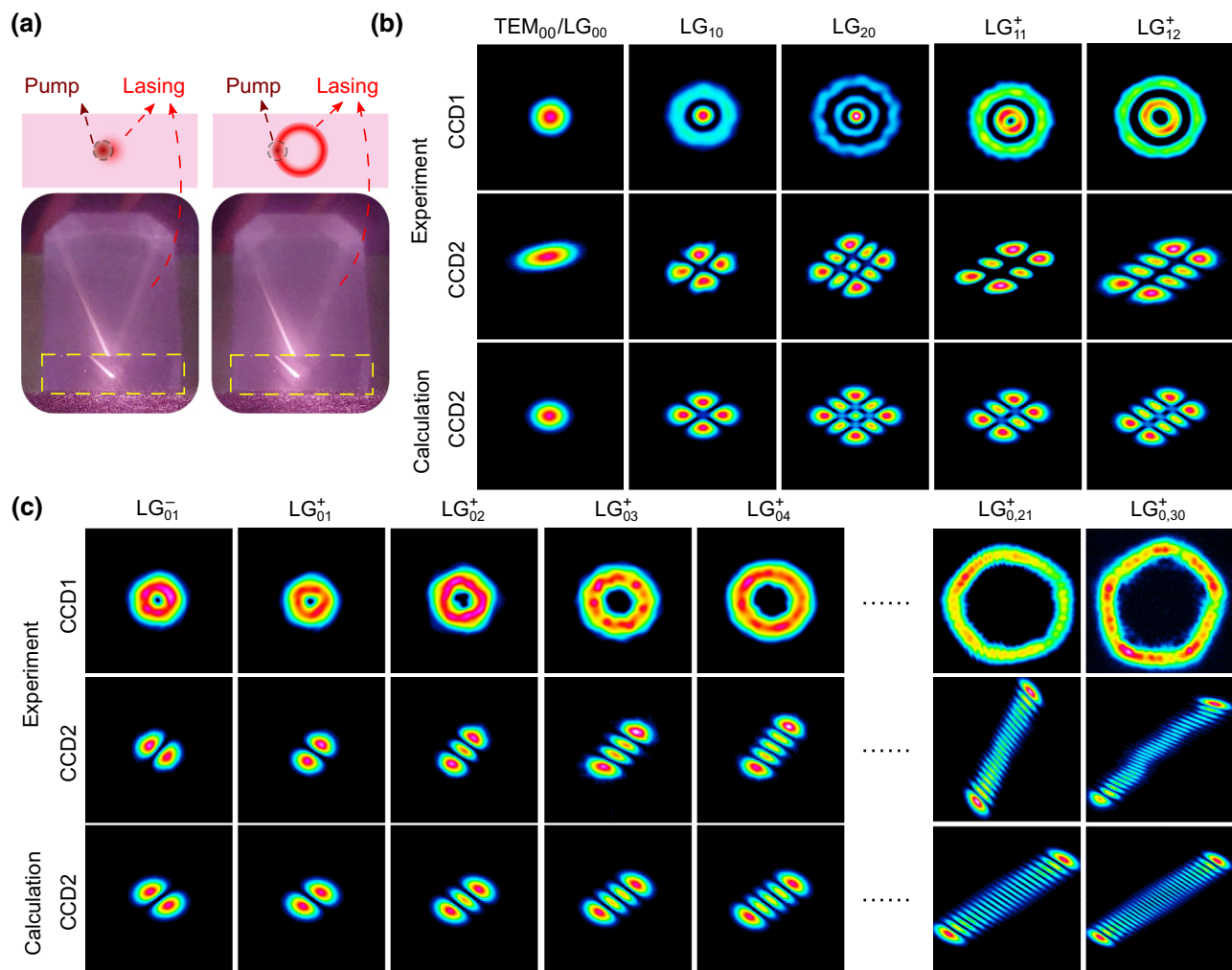
FIG. 2. (a) Illustration of the overlap positions of excited lasing and pump beams on the input facet of the laser cavity (above), photographs of the cavity on operation with observable beam width changes for the intracavity lasing beams (below). Observation of the original beam profiles in CCD1 and the experimental and theoretically calculated results for the converted beam profiles in CCD2: (b) fundamental Gaussian and LG modes with radial mode orders $p = 1, 2$; (c) Vortex beams ($LG_{0,\ell}$ modes with ℓ up to 30). Note: beam profiles in CCD2 are used to determine the mode indices and the topological charges of vortex beams.

of $p + 1$, while the number of the spots in each array is equal to the value of $|\ell| + p + 1$. As a result, both indices values of p and ℓ are identified. The orientation of the tilting gives the sign of the topological charge ℓ. In the simple case of vortex beams with $p = 0$, only one array is observed with the number of spots equal to $|\ell| + 1$. Therefore, this method helps to determine mode indices of these beams. Note that different methods to determine the topological charge of an OAM beam have been developed. For instance, one can use a simple forklike interferogram method based on a planar-concave lens [58] or diffraction pattern mapping through a single slit [61].

OAM beams with ℓ up to 30 have been observed in this experiment. The corresponding relative position of the pump beam for $LG_{0,30}^+$ is about 0.97 mm offset from the center of the input facet of the cavity as shown in Appendix A. Considering the dimension of the cavity, we believe that generating vortex beams carrying much larger OAM is still feasible. Laser performances concerning the conversion efficiency and the threshold pump power are also measured for several lasing modes from the fundamental one to high-order vortex beams as shown in Fig. 3. For LG_{00}, LG_{01}^+, LG_{02}^+, LG_{03}^+, $LG_{0,10}^+$, $LG_{0,20}^+$, and $LG_{0,30}^+$ lasing modes, the pump thresholds are about 47, 98, 110, 123, 205, 237, and 255 mW, respectively, while the slope efficiencies are about 45, 41, 41, 35, 28, 23, and 20%, respectively. One sees that the threshold pump power increases while the slope efficiency decreases for exciting higher-order lasing modes. Because we use a regular Gaussian pump beam to excite the doughnut-shape OAM lasing
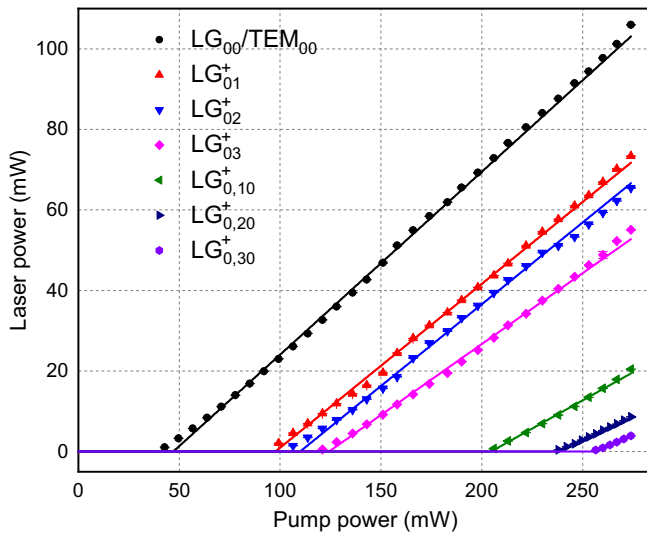
FIG. 3. Slope efficiency data for LG_{00}, LG_{01}^+, LG_{02}^+, LG_{03}^+, $LG_{0,10}^+$, $LG_{0,20}^+$, and $LG_{0,30}^+$ lasing modes. Linear fits give the absorbed threshold pump power and the slope efficiency values of 47.0 mW, 45%, 98 mW, 41%, 110 mW, 41%, 123 mW, 35%, 205 mW, 28%, 237 mW, 23% and 255 mW, 20% for these lasing modes, respectively.
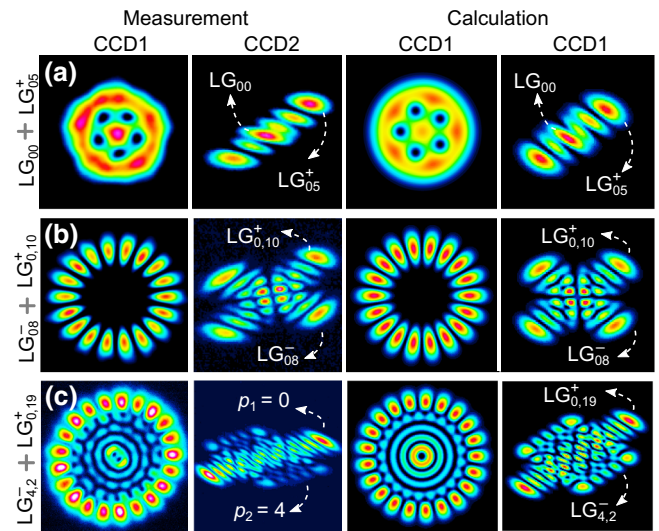

FIG. 4. Observation of the superposition of OAM lasing modes: (a) $LG_{00} + LG_{05}^+$ (vortex crystals), (b) $LG_{0,10}^+ + LG_{0,8}^-$ (petal patterns) and (c) $LG_{4,2}^-$ and $LG_{0,19}^+$. Left: the experimental results from CCD1 and CCD2; Right: the corresponding calculated patterns.

mode, the spatial mode overlap conditions between the pump and high-order lasing modes lead to larger threshold pump power as compared to the fundamental lasing mode. Note that contamination of the crystal surface would lead to an increased laser threshold and difficulty to harness the direct output of vortex beams carrying very large OAM.

In addition, we observe the superposition of different LG mode pairs with degenerate eigenfrequencies in the non-planar cavity configuration as shown in Figs. 4(a) and 4(b). We obtain vortex beams carrying OAM crystals indicating crystallike singularity points in the wavefront similar to the observation in a vertical-cavity surface-emitting semiconductor laser [62]. Figure 4(a) shows an example of our observation. The experimental beam profiles on both CCD1 and CCD2 match our theoretical expectation using Eqs. (1) and (2). The converted profile in CCD2 is used to identify the mode components of this superposition. Considering the forklike interferogram obtained using a plano-concave lens [58], the converted method using a tilted lens clearly reveals and confirms the mode composition of the lasing mode being the superposition of a fundamental mode LG_{00} and a higher-order vortex mode LG_{05}^+. Moreover, we also obtain the superposition of LG vortex modes with opposite signs of topological charge ℓ, leading to a petallike beam profile also shown in Fig. 4(b). By matching the calculation with the experimental one, we find that this beam is actually the superposition of $LG_{0,10}^+$ and $LG_{0,8}^-$, not $LG_{0,9}^\pm$, although they share similar

transverse beam profiles. It should be noted that the superposition of lasing modes relies strongly on the pumping beam condition and the cavity eigenmode frequency that are decided by the cavity geometry. Such superposition of vortex modes can facilitate the application of rotational Doppler shift for measuring the angular speed of a spinning object [63,64].

However, we only observe a few sets of superposition modes, which could be due to the fact that these superposition modes are determined by the geometry of the cavity itself [55] and the lasing action would also require sufficient pump power that is decided by the mode overlap condition between the pump and the lasing mode. Nevertheless, we observe another superposition of lasing modes as shown in Fig. 4(c). Note that the spot number of the outer ring is determined by the sum of the absolute values of topological charges $|\ell_1| + |\ell_2|$, while the central hole patterns in this figure gives the absolute topological charge value $|\ell_2|$. The radial orders p_1 and p_2, on the other hand, can be obtained from the transformed pattern in CCD2. We can thereby recognize the composition of this beam being the superposition of $LG_{4,2}^-$ and $LG_{0,19}^+$. Note that the central holes in CCD1 could be induced by possible mode distortions.

Note that we have previously developed a simple forklike interferogram method to determine the topological charge of an OAM beam using a planar-concave lens [58]. Although the previous method can give directly the topological charge information of spatially separated vortices [59], it cannot be used to identify vortex beams carrying

large OAM. A comparison between these two methods is presented in Appendix B.

IV. SINGLE-FREQUENCY LASING PERFORMANCE

Beside the simplicity and rigidity of the versatile monolithic OAM beam-emission platform, another attractive feature is its ability to produce low-noise single-frequency and single-directional laser sources. Here, we characterize the frequency noise performance of a vortex laser beam LG_{01} as shown in Fig. 5. The frequency noise spectrum is obtained using a fast photodiode and a phase noise analyzer (R&S FSWP26). A packaged laser head emitting single-frequency LG_{00} mode beams is chosen as the reference. The photo and beat linewidth of the packaged laser head can be found in Appendix C. The single-sideband phase noise $\mathcal{L}(f)$ of an OAM beam (LG_{01}) compared with the reference as a rf beatnote is first recorded. We then convert $\mathcal{L}(f)$ into the corresponding frequency noise (in Hz/Hz$^{1/2}$) using its power spectral density $S_\nu(f)$ (in Hz^2/Hz):

$$S_\nu(f) = 2f^2 10^{\mathcal{L}(f)/10}, \tag{3}$$

where f is the frequency offset from the carrier.

Figure 5 shows the corresponding frequency noise spectrum (in Hz/Hz$^{1/2}$) of our OAM laser. The noise floor of the OAM laser reaches the level of 0.1 Hz/Hz$^{1/2}$ at frequency offset above a few hundred kHz. The instantaneous linewidth can thereby be estimated using $\Delta f = \pi S_\nu$ [65,66], where S_ν is the floor of the power spectral density and thus the square of the frequency noise floor in Fig. 5. Therefore, we expect that an instantaneous linewidth Δf less than 0.1 Hz has been achieved resulting from the
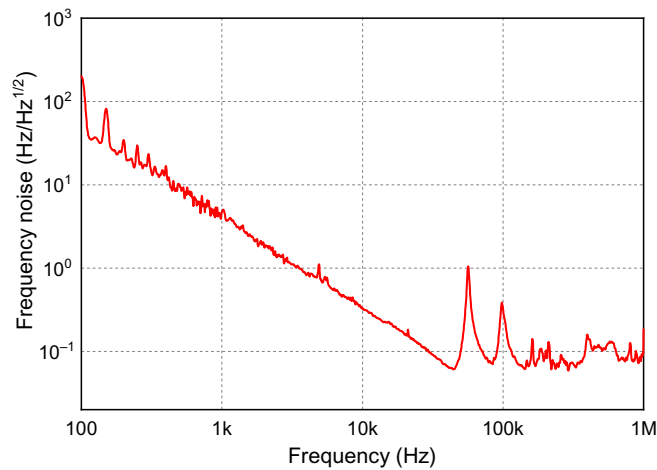

FIG. 5. Frequency noise spectrum of a typical LG_{01} OAM laser. The spectrum is obtained by beating the oscillator with a packaged fundamental mode laser, which uses the cavity with the same geometry.

nature advantage of the monolithic and high-quality platform. This is the direct OAM laser featuring the narrowest instantaneous linewidth. Two main peaks are observed in the frequency noise spectrum, which are related to the relaxation oscillations of two Nd:YAG lasers at LG_{01} and LG_{00}, respectively. In principle, a noise eater circuit can be further added to suppress this noise contribution for applications that are sensitive in this frequency domain.

It should be noted that the laser linewidth is related to various time-dependent jitter components such as mechanical, thermal, and electrical fluctuations in a laser. Therefore, direct measurement by heterodyne beating is strongly dependent on the time scale. The instantaneous linewidth here means the linewidth measurement at a fast time scale. This value is thereby usually estimated from the floor of the power spectral density of frequency noise. Nevertheless, it is still limited by the Schawlow-Townes linewidth [67,68]

$$\Delta\nu = \frac{\pi h \nu^3}{P Q_c^2}, \tag{4}$$

where h is the Planck constant, ν is the laser frequency, P is the output power, and Q_c is the cold cavity quality factor. Considering the reflectivity of 99.5% at 1064 nm for the coated facet of the cavity and the roundtrip path of about 30 mm, the corresponding cold cavity Q_c at the lasing wavelength would be 3.5×10^7. If we assume a laser beam with output power of 10 mW, the according Schawlow-Townes linewidth would be about 4 mHz. The larger instantaneous linewidth value we obtain means that it is still limited by technical noises and possible parasitic loss in the cavity.

V. DUAL-FREQUENCY LASING

By adjusting the relative position of the pump beam on the cavity, we also demonstrate the direction generation of a dual-frequency OAM laser beam from the compact oscillator. Dual-frequency lasing with different frequency spacing in the order of a few GHz are observed. The formation of dual-frequency lasing could result from different mode compositions lasing at different wavelengths. Figure 6 gives an example of the lasing signals detected through the scanning FP interferometer. The transition from single-frequency lasing to dual-frequency lasing is recorded. We find that by placing the pump-beam position between two optimal positions for single-frequency lasing separately at mode LG_{01}^+ and LG_{01}^-. One can obtain stable dual-frequency lasing at both modes. In comparison to single-frequency lasing with pedal patterns such as Fig. 4(b), the beam profile of dual-frequency dual-mode lasing does not show the similar pattern since two lasing modes have different lasing wavelengths and thus do not interfere with each other.
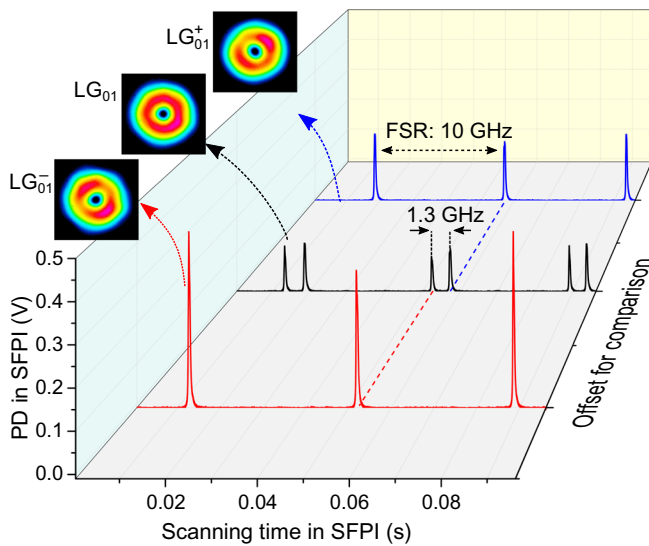
FIG. 6.   Laser signals in the scanning FP interferometer (SFPI). Black curve: dual-frequency lasing with spacing of 1.3 GHz. Red and blue curves: single-frequency lasing corresponding to two frequency components. The free spectral range (FSR) of the scanning FP interferometer is 10 GHz. Inset: the corresponding original beam profiles.

FIG. 7.   (a) Optical spectrum of a dual-frequency OAM laser LG_{02}. Insets: the corresponding beam profile (left) and an enlargement of the dual peak. (b) Transmitted signal spectrum in a scanning Fabry-Perot interferometer.

As these two modes share very similar roundtrip passes in the compact cavity, we expect that a natural common-mode noise suppression exists and would lead to low phase noise. We thereby further send the dual-frequency laser signal into a fast photodiode for examining the phase noise of the beatnote signal. The generated rf signal is inspected with a signal and spectrum analyzer and a phase-noise analyzer. The dual-frequency lasing with the lowest phase noise in our experiment is from LG_{02} modes. The optical spectrum is recorded using an optical spectrum analyzer as shown in Fig. 7(a). The inset (left) gives its transverse-beam profile, while the inset (right) shows an enlargement of its optical spectrum. The wavelength spacing of the dual-frequency laser is about 0.03 nm. The spacing is also investigated using a free-space scanning FP interferometer, whose transmission spectrum is presented in Fig. 7(b), giving a more accurate frequency spacing of about 8.2 GHz. It should be noted that the dual-frequency lasing is dependent on both the relative position of the pump beam and the pump-power condition.

Figure 8 shows its phase-noise performance spectrum. The inset is the beatnote spectrum around a peak frequency at 8.217 GHz corresponding to the X band of the microwave frequency domain. The measured phase noise reaches -118 dBc/Hz at 10 kHz and a floor -145 dBc/Hz above 500 kHz. The low phase noise of the generated rf signal also reflects the high-performance nature of the dual-frequency laser source. It should be noted that we also observe dual-frequency lasing with other different frequency spacings even above 10 GHz. The phase-noise
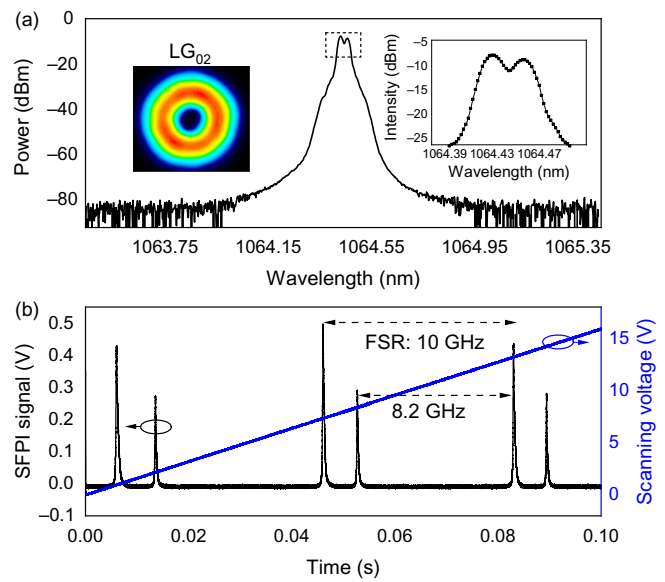
performance differs from each other, which is dependent on the degree of common-mode noise suppression. The monolithic nonplanar ring solid-state dual-frequency lasing, different from the reported dual-frequency lasing platforms using fibers [69] or vertical-external-cavity surface-emitting lasers (VECSELs) using fully correlated pumping [70], features lower phase-noise performance as listed in Table I. It thereby shows an alternative way to generate low-noise dual-frequency compact lasers for
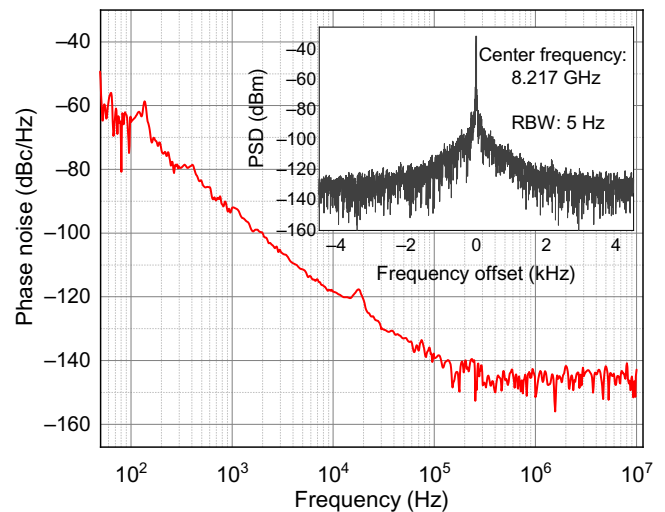

FIG. 8.   Phase noise of the rf signal generated by sending the dual-frequency signal to a fast photodiode. Inset: the corresponding rf spectrum with resolution bandwidth (RBW) at 5 Hz.

TABLE I. Comparison of phase-noise performances at 10-kHz offset frequency for the rf beatnote of dual-frequency lasers using different types of lasing techniques.

Types	Wavelength	Beatnote	Phase noise @10 kHz
DFB fiber [69]	1547 nm	10 GHz	−75 dBc/Hz
VECSELs [70]	1568 nm	<3 GHz	> −100 dBc/Hz
This work	1064 nm	8.2 GHz	−118 dBc/Hz

potential dual-frequency Doppler lidar [71]. Interestingly, the OAM feature of the vortex beam can also bring along additional potential applications for such laser sources.

VI. CONCLUSIONS

Compared with other methods to generate LG vortex beams such as using SLM, although the oscillator method is lack of flexibility and versatility, it provides a compact solution for the direct generation of very low-noise vortex beams. Moreover, this kind of monolithic nonplanar ring-cavity structure can withstand the harsh aerospace environment. For instance, low-noise fundamental mode lasers based on such cavities have been successfully used as high-coherent light sources for several satellite missions including GRACE Follow-On and LISA Pathfinder [72]. Our finding combines the advantage of such rigid cavities with vortex beams carrying orbital angular momentum. It is applicable to other lasing wavelengths when different types of gain materials are used. The continuous-wave lasing with a sub-Hz instantaneous linewidth shows that such vortex beams are highly coherent and can find applications in high-capacity optical communication, laser gyros, laser ranging, and quantum-information processing. Moreover, we also demonstrate dual-frequency lasing carrying orbital angular momentum. This finding can also be further explored in versatile applications using dual-frequency lasers such as Doppler lidar systems.

APPENDIX A: RELATIVE POSITIONS OF THE PUMP BEAM ON THE INPUT FACET FOR DIFFERENT LASING MODES

To show an example of the dependence of various lasing modes on the relative positions of the pump beam on the input facet of the nonplanar ring orbital angular momentum oscillator, we map the position of the cavity by adjusting the two-dimensional translation stage. The
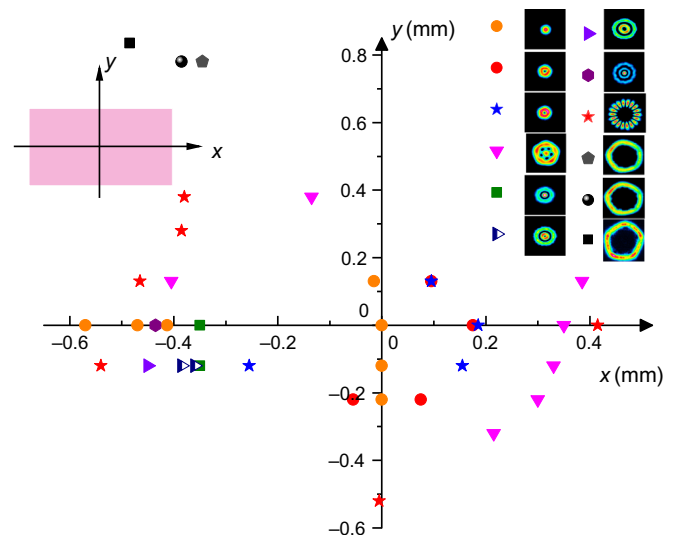

FIG. 9. Relative positions of the pump laser beam on the input facet for different LG mode lasing modes from top to bottom and from left to right: LG_{00}, $LG_{01}^{\pm}$, $LG_{00} + LG_{05}^{+}$, LG_{10}, LG_{11}^{+}, LG_{12}^{+}, LG_{20}, $LG_{0,10}^{+} + LG_{08}^{-}$, $LG_{0,20}^{+}$, $LG_{0,22}^{+}$, $LG_{0,30}^{+}$. Inset: illustration of the coordinate axes on the input facet of the cavity.

center position is defined at the optimized position where the threshold reaches minimum for the fundamental lasing mode. An example of the result is shown in Fig. 9. It should be noted that a few micrometers change in the position of the pump beam can switch the sign of the topological charge of LG01 modes, while it would take a few tens of micrometers for twisted light beams with large topological charges.

APPENDIX B: COMPARISON OF TWO SIMPLE METHODS FOR PROBING OAM BEAMS

We further compare two simple methods on measuring topological charges of OAM lasing beams from $LG_{01}^{\pm}$ and $LG_{00} + LG_{05}^{+}$ modes. Figures 10(a) and 10(b) illustrate the setups of these methods using a plano-concave lens and a tilted biconvex spherical lens, respectively. The former method developed by Lin *et al.* uses the interferometry way to generate forklike fringes for detection [58]. Beam I is the reflected light from the plane surface, while beam II is the second reflected light that diverges after it reflects off the concave surface. By adjusting the position and incident angle of the beam on the lens, one can overlap two beams into a CCD and record the interference patterns as shown in the inset of Fig. 10(a). The latter method used in this experiment was developed by Vaity *et al.* [60]. The experimental results are shown in Fig. 10(c). One can see that the interferogram method can show clearly the direction of each "fork," while the conversion method, on the other hand, can reveal the composition of the vortex crystal beam being the superposition of $LG_{00} + LG_{05}^{+}$.
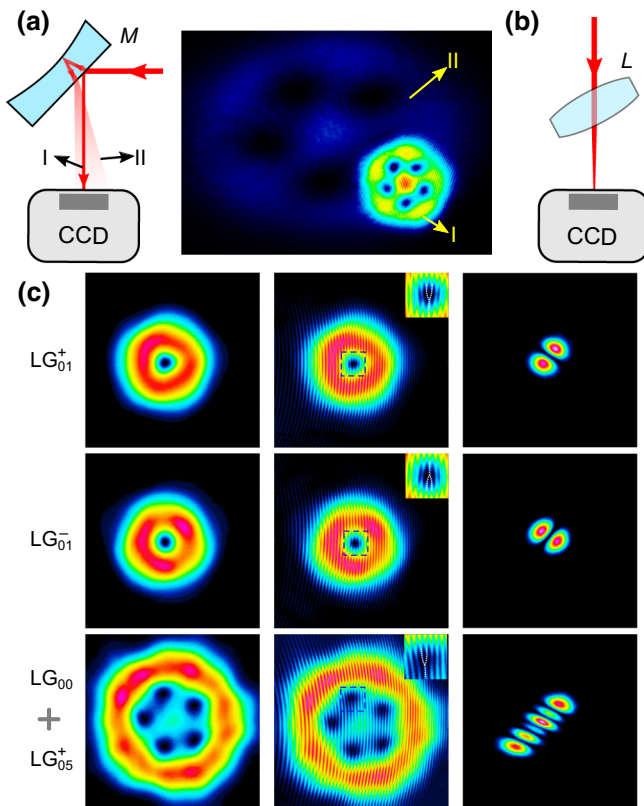
FIG. 10. Comparison of two simple methods on measuring the topological charge of a OAM beam. (a) Illustration of the fork interferogram method using a plano-concave lens. (b) Illustration of the simple transformation method using a tilted biconvex spherical lens. (c) Comparison of the measurement results for different OAM laser beams from top to bottom: LG_{01}^+, LG_{01}^- and $LG_{00} + LG_{05}^+$ beams. Left, original beam profiles; middle, the interferometry method using a plano-concave lens as a reflector; right, the transformation method using a tilted lens.

APPENDIX C: A PACKAGED LASER HEAD

We design and package a nonplanar ring-laser head that outputs a single-frequency fundamental Gaussian beam as shown in Fig. 11(a). A thermistor and a Peltier thermo-electric cooler (TEC) are implemented for the temperature control of the cavity. A piezoelectric actuator is also attached to the top surface of the cavity for fast tuning the laser wavelength. Two single-mode fiber mating sleeves are fixed for pump input and laser output through fibers, respectively. The output laser beam inside the laser head is set to be linearly polarized using a quarter-wave plate and a half-wave plate. The orientation of the polarization is designed for a polarization maintaining output fiber. Figure 11(b) presents a typical beatnote spectrum of such a laser showing kHz-level beat linewidth. This packaged laser is used as a reference laser beam for measuring the linewidth of OAM beams. It should be noted that the laser head can also be altered for the free-space OAM beam output.
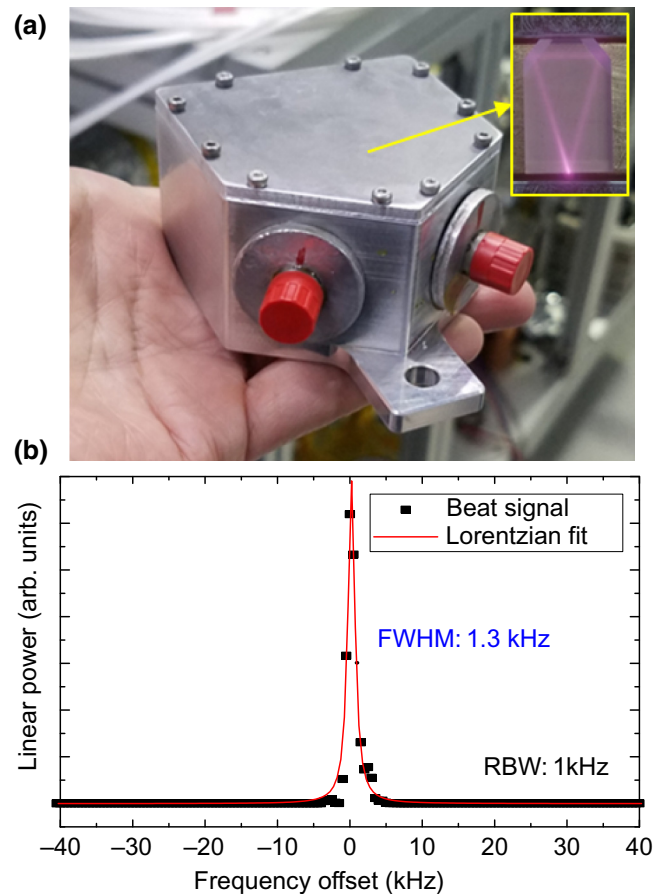

FIG. 11. (a) Example of a packaged laser head with a pump fiber-input port and a polarization-maintaining fiber-output port. Inset: photo of the Nd:YAG cavity. (b) Example of the beat-note spectrum between two fundamental mode lasers showing a Lorentzian fitted linewidth of about 1.3 kHz.

[1] L. Allen, M. W. Beijersbergen, R. Spreeuw, and J. Woerd-man, Orbital angular momentum of light and the transformation of Laguerre-Gaussian laser modes, Phys. Rev. A **45**, 8185 (1992).

[2] A. M. Yao and M. J. Padgett, Orbital angular momentum: Origins, behavior and applications, Adv. Opt. Photon. **3**, 161 (2011).

[3] K. Y. Bliokh and F. Nori, Transverse and longitudinal angular momenta of light, Phys. Rep. **592**, 1 (2015).

[4] A. E. Willner, H. Huang, Y. Yan, Y. Ren, N. Ahmed, G. Xie, C. Bao, L. Li, Y. Cao, Z. Zhao, J. Wang, M. P. J. Lavery, M. Tur, S. Ramachandran, A. F. Molisch, N. Ashrafi, and S. Ashrafi, Optical communications using orbital angular momentum beams, Adv. Opt. Photon. **7**, 66 (2015).

[5] J. Wang, Advances in communications using optical vortices, Photon. Res. **4**, B14 (2016).

[6] H. Rubinsztein-Dunlop, A. Forbes, M. V. Berry, M. R. Dennis, D. L. Andrews, M. Mansuripur, C. Denz, C. Alpmann, P. Banzer, T. Bauer *et al.*, Roadmap on structured light, J. Opt. **19**, 013001 (2016).

[7] M. J. Padgett, Orbital angular momentum 25 years on, Opt. Express **25,** 11265 (2017).

[8] M. Erhard, R. Fickler, M. Krenn, and A. Zeilinger, Twisted photons: New quantum perspectives in high dimensions, Light Sci. Appl. **7,** 17146 (2018).

[9] C. Rosales-Guzmán, B. Ndagano, and A. Forbes, A review of complex vector light fields and their applications, J. Opt. **20,** 123001 (2018).

[10] Y. Shen, X. Wang, Z. Xie, C. Min, X. Fu, Q. Liu, M. Gong, and X. Yuan, Optical vortices 30 years on: OAM manipulation from topological charge to multiple singularities, Light: Sci. Appl. **8,** 90 (2019).

[11] G. Gibson, J. Courtial, M. J. Padgett, M. Vasnetsov, V. Pas'ko, S. M. Barnett, and S. Franke-Arnold, Free-space information transfer using light beams carrying orbital angular momentum, Opt. Express **12,** 5448 (2004).

[12] J. Wang, J. Y. Yang, I. M. Fazal, N. Ahmed, Y. Yan, H. Huang, Y. Ren, Y. Yue, S. Dolinar, and M. Tur, Terabit free-space data transmission employing orbital angular momentum multiplexing, Nat. Photonics **6,** 488 (2012).

[13] N. Bozinovic, Y. Yue, Y. Ren, M. Tur, P. Kristensen, H. Huang, A. E. Willner, and S. Ramachandran, Terabit-scale orbital angular momentum mode division multiplexing in fibers, Science **340,** 1545 (2013).

[14] A. Sit, F. Bouchard, R. Fickler, J. Gagnon-Bischoff, H. Larocque, K. Heshami, D. Elser, C. Peuntinger, K. Günthner, B. Heim, C. Marquardt, G. Leuchs, R. W. Boyd, and E. Karimi, High-dimensional intracity quantum cryptography with structured photons, Optica **4,** 1006 (2017).

[15] D. Cozzolino, D. Bacco, B. Da Lio, K. Ingerslev, Y. Ding, K. Dalgaard, P. Kristensen, M. Galili, K. Rottwitt, S. Ramachandran, and L. K. Oxenløwe, Orbital Angular Momentum States Enabling Fiber-Based High-Dimensional Quantum Communication, Phys. Rev. Appl. **11,** 064058 (2019).

[16] A. Mair, A. Vaziri, G. Weihs, and A. Zeilinger, Entanglement of the orbital angular momentum states of photons, Nature **412,** 313 (2001).

[17] A. Nicolas, L. Veissier, L. Giner, E. Giacobino, D. Maxein, and J. Laurat, A quantum memory for orbital angular momentum photonic qubits, Nat. Photonics **8,** 234 (2014).

[18] D.-S. Ding, W. Zhang, Z.-Y. Zhou, S. Shi, G.-Y. Xiang, X.-S. Wang, Y.-K. Jiang, B.-S. Shi, and G.-C. Guo, Quantum Storage of Orbital Angular Momentum Entanglement in an Atomic Ensemble, Phys. Rev. Lett. **114,** 050502 (2015).

[19] P.-A. Moreau, E. Toninelli, T. Gregory, R. S. Aspden, P. A. Morris, and M. J. Padgett, Imaging Bell-type nonlocal behavior, Sci. Adv. **5,** eaaw2563 (2019).

[20] M. Padgett and R. Bowman, Tweezers with a twist, Nat. Photonics **5,** 343 (2011).

[21] S. W. Hell, Toward fluorescence nanoscopy, Nat. Biotechnol. **21,** 1347 (2003).

[22] K. Toyoda, K. Miyamoto, N. Aoki, R. Morita, and T. Omatsu, Using optical vortex to control the chirality of twisted metal nanostructures, Nano Lett. **12,** 3645 (2012).

[23] T. Omatsu, K. Miyamoto, K. Toyoda, R. Morita, Y. Arita, and K. Dholakia, A new twist for materials science: The formation of chiral structures using the angular momentum of light, Adv. Opt. Mater. **7,** 1801672 (2019).

[24] A. Bag, M. Neugebauer, P. Woźniak, G. Leuchs, and P. Banzer, Transverse Kerker Scattering for Angstrom Localization of Nanoparticles, Phys. Rev. Lett. **121,** 193902 (2018).

[25] A. Forbes, Structured light from lasers, Laser Photonics Rev. **13,** 1900140 (2019).

[26] S. Pachava, R. Dharmavarapu, A. Vijayakumar, S. Jayakumar, A. Manthalkar, A. Dixit, N. K. Viswanathan, B. Srinivasan, and S. Bhattacharya, Generation and decomposition of scalar and vector modes carrying orbital angular momentum: A review, Opt. Eng. **59,** 1 (2019).

[27] T. Omatsu, K. Miyamoto, and A. J. Lee, Wavelength-versatile optical vortex lasers, J. Opt. **19,** 123002 (2017).

[28] X. Wang, Z. Nie, Y. Liang, J. Wang, T. Li, and B. Jia, Recent advances on optical vortex generation, Nanophotonics **7,** 1533 (2018).

[29] M. W. Beijersbergen, L. Allen, H. Van der Veen, and J. Woerdman, Astigmatic laser mode converters and transfer of orbital angular momentum, Opt. Commun. **96,** 123 (1993).

[30] C. He, J. Chang, Q. Hu, J. Wang, J. Antonello, H. He, S. Liu, J. Lin, B. Dai, D. S. Elson *et al.*, Complex vectorial optics through gradient index lens cascades, Nat. Commun. **10,** 1 (2019).

[31] M. Beijersbergen, R. Coerwinkel, M. Kristensen, and J. Woerdman, Helical-wavefront laser beams produced with a spiral phaseplate, Opt. Commun. **112,** 321 (1994).

[32] N. R. Heckenberg, R. McDuff, C. P. Smith, and A. G. White, Generation of optical phase singularities by computer-generated holograms, Opt. Lett. **17,** 221 (1992).

[33] R. Barboza, U. Bortolozzo, M. G. Clerc, S. Residori, and E. Vidal-Henriquez, Optical vortex induction via light-matter interaction in liquid-crystal media, Adv. Opt. Photonics **7,** 635 (2015).

[34] A. Rubano, F. Cardano, B. Piccirillo, and L. Marrucci, Q-plate technology: A progress review, J. Opt. Soc. Am. B **36,** D70 (2019).

[35] N. Yu and F. Capasso, Flat optics with designer metasurfaces, Nat. Mater. **13,** 139 (2014).

[36] M. L. Chen, L. J. Jiang, and W. E. Sha, Orbital angular momentum generation and detection by geometric-phase based metasurfaces, Appl. Sci. **8,** 362 (2018).

[37] C. Xinlun, J. Wang, M. J. Strain, B. Johnson-Morris, J. Zhu, M. Sorel, J. L. O'Brien, M. G. Thompson, and S. Yu, Integrated compact optical vortex beam emitters, Science **338,** 363 (2012).

[38] E. Ostrovsky, K. Cohen, S. Tsesses, B. Gjonaj, and G. Bartal, Nanoscale control over optical singularities, Optica **5,** 283 (2018).

[39] M. Wang, R. Salut, H. Lu, M.-A. Suarez, N. Martin, and T. Grosjean, Subwavelength polarization optics via individual and coupled helical traveling-wave nanoantennas, Light Sci. Appl. **8,** 1 (2019).

[40] A. Forbes, A. Dudley, and M. McLaren, Creation and detection of optical modes with spatial light modulators, Adv. Opt. Photonics **8,** 200 (2016).

[41] M. Mirhosseini, O. S. Magaña Loaiza, C. Chen, B. Rodenburg, M. Malik, and R. W. Boyd, Rapid generation of light beams carrying orbital angular momentum, Opt. Express **21,** 30196 (2013).

[42] S. Ngcobo, I. Litvin, L. Burger, and A. Forbes, A digital laser for on-demand laser modes, Nat. Commun. **4,** 2289 (2013).

[43] P. Miao, Z. Zhang, J. Sun, W. Walasik, S. Longhi, N. M. Litchinitser, and L. Feng, Orbital angular momentum microlaser, Science **353,** 464 (2016).

[44] J. A. Rivera, T. C. Galvin, A. W. Steinforth, and J. G. Eden, Fractal modes and multi-beam generation from hybrid microlaser resonators, Nat. Commun. **9,** 2594 (2018).

[45] Q. Zhen, X. Guoqiang, W. Yuhang, Y. Peng, M. Jingui, Q. Liejia, and F. Dianyuan, Generating high-charge optical vortices directly from laser up to 288th order, Laser Photonics Rev. **12,** 1800019 (2018).

[46] G. Lin and Y. K. Chembo, Monolithic total internal reflection resonators for applications in photonics, Opt. Mater. X **2,** 100017 (2019).

[47] G. Lin, A. Coillet, and Y. K. Chembo, Nonlinear photonics with high-Q whispering-gallery-mode resonators, Adv. Opt. Photonics **9,** 828 (2017).

[48] G. Lin, J. U. Fürst, D. V. Strekalov, and N. Yu, Wide-range cyclic phase matching and second harmonic generation in whispering gallery resonators, Appl. Phys. Lett. **103,** 181107 (2013).

[49] G. Lin, S. Diallo, J. M. Dudley, and Y. K. Chembo, Universal nonlinear scattering in ultra-high Q whispering gallery-mode resonators, Opt. Express **24,** 14880 (2016).

[50] T. J. Kane and R. L. Byer, Monolithic, unidirectional single-mode Nd:YAG ring laser, Opt. Lett. **10,** 65 (1985).

[51] A. C. Nilsson, E. K. Gustafson, and R. L. Byer, Eigenpolarization theory of monolithic nonplanar ring oscillators, IEEE J. Quantum Electron. **25,** 767 (1989).

[52] G. M. Harry, L. S. Collaboration *et al.*, Advanced LIGO: The next generation of gravitational wave detectors, Class. Quantum Gravity **27,** 084006 (2010).

[53] B. S. Sheard, G. Heinzel, K. Danzmann, D. A. Shaddock, W. M. Klipstein, and W. M. Folkner, Intersatellite laser ranging instrument for the GRACE follow-on mission, J. Geod. **86,** 1083 (2012).

[54] A. V. Smith and D. J. Armstrong, Generation of vortex beams by an image-rotating optical parametric oscillator, Opt. Express **11,** 868 (2003).

[55] N. Schine, A. Ryou, A. Gromov, A. Sommer, and J. Simon, Synthetic Landau levels for photons, Nature **534,** 671 (2016), arXiv:1511.07381.

[56] B. Sorazu, P. Fulda, B. Barr, A. Bell, C. Bond, L. Carbone, A. Freise, S. Hild, S. Huttner, J. Macarthur *et al.*, Experimental test of higher-order Laguerre-Gauss modes in the 10 m Glasgow prototype interferometer, Class. Quantum Gravity **30,** 035004 (2013).

[57] A. Noack, C. Bogan, and B. Willke, Higher-order Laguerre-Gauss modes in (non-) planar four-mirror cavities for future gravitational wave detectors, Opt. Lett. **42,** 751 (2017).

[58] G. Lin, Y. Cao, R. Ji, C. Hou, and Z. Lu, Direct generation of a narrow-linewidth Laguerre-Gaussian vortex laser in a monolithic nonplanar oscillator, Opt. Lett. **43,** 4164 (2018).

[59] G. Lin, Y. Cao, Z. Lu, and Y. K. Chembo, Spontaneous generation of orbital angular momentum crystals using a monolithic Nd:YAG nonplanar ring laser, Opt. Lett. **44,** 203 (2019).

[60] P. Vaity, J. Banerji, and R. Singh, Measuring the topological charge of an optical vortex by using a tilted convex lens, Phys. Lett. A **377,** 1154 (2013).

[61] J. P. C. Narag and N. Hermosa, Probing Higher Orbital Angular Momentum of Laguerre-Gaussian Beams via Diffraction Through a Translated Single Slit, Phys. Rev. Appl. **11,** 054025 (2019).

[62] J. Scheuer and M. Orenstein, Optical vortices crystals: Spontaneous generation in nonlinear semiconductor microcavities, Science **285,** 230 (1999).

[63] H.-L. Zhou, D.-Z. Fu, J.-J. Dong, P. Zhang, D.-X. Chen, X.-L. Cai, F.-L. Li, and X.-L. Zhang, Orbital angular momentum complex spectrum analyzer for vortex light based on the rotational doppler effect, Light Sci. Appl. **6,** e16251 (2017).

[64] M. P. Lavery, F. C. Speirits, S. M. Barnett, and M. J. Padgett, Detection of a spinning object using light's orbital angular momentum, Science **341,** 537 (2013).

[65] W. Liang, V. Ilchenko, D. Eliyahu, A. Savchenkov, A. Matsko, D. Seidel, and L. Maleki, Ultralow noise miniature external cavity semiconductor laser, Nat. Commun. **6,** 7371 (2015).

[66] S. Gundavarapu, G. M. Brodnik, M. Puckett, T. Huffman, D. Bose, R. Behunin, J. Wu, T. Qiu, C. Pinho, N. Chauhan *et al.*, Sub-hertz fundamental linewidth photonic integrated Brillouin laser, Nat. Photonics **13,** 60 (2019).

[67] M. Lax, Classical noise. V. Noise in self-sustained oscillators, Phys. Rev. **160,** 290 (1967).

[68] A. L. Schawlow and C. H. Townes, Infrared and optical masers, Phys. Rev. **112,** 1940 (1958).

[69] M. Guionie, L. Frein, A. Carré, G. Loas, F. Bondu, E. Pinsard, L. Lablonde, B. Cadier, M. Alouini, M. Romanelli *et al.*, Beat note stabilization in dual-polarization DFB fiber lasers by an optical phase-locked loop, Opt. Express **26,** 3483 (2018).

[70] H. Liu, G. Gredat, S. De, I. Fsaifes, A. Ly, R. Vatré, G. Baili, S. Bouchoule, F. Goldfarb, and F. Bretenaker, Ultra-low noise dual-frequency VECSEL at telecom wavelength using fully correlated pumping, Opt. Lett. **43,** 1794 (2018).

[71] L. Morvan, N. D. Lai, D. Dolfi, J.-P. Huignard, M. Brunel, F. Bretenaker, and A. L. Floch, Building blocks for a two-frequency laser lidar-radar: A preliminary study, Appl. Opt. **41,** 5702 (2002).

[72] P. McNamara, S. Vitale, and K. Danzmann, LISA pathfinder, Classical Quantum Gravity **25,** 114034 (2008).